



# Storm sudden commencement and its effect on high-latitude HF communication links

S. E. Ritchie<sup>1,2</sup> and F. Honary<sup>2</sup>

Received 18 December 2008; revised 14 February 2009; accepted 8 March 2009; published 25 June 2009.

[1] Following particle precipitation at high latitudes that occurs as a result of geomagnetic disturbances, the electron density of the *E* region of the ionosphere undergoes substantial variation. These variations modify the *E* layer propagation characteristics which adversely affect HF propagation paths both unexpectedly and in many cases for long periods of time. This paper presents two case studies of how the enhancement of *E* region electron density immediately following storm sudden commencement affects high-latitude HF communications links in and through the auroral zone. Using data gathered from ionosondes, incoherent scatter radar and an oblique sounder, the Advanced Composition Explorer Satellite, and riometers and magnetometers, the physical effects of particle precipitation on the ionospheric *E* layer and the resulting effect on HF links is revealed. Both case studies show that besides the expected occurrence of severe short-term absorption and the reduction in the critical frequency of the *F* layer caused by a redistribution of the electron density in the upper layers of the ionosphere, there is the likelihood a sporadic *E* layer will form and/or be enhanced because of significant and sustained particle precipitation. When the critical frequency of the sporadic *E* layer increases above the norm and in cases exceeds the critical frequency of the *F* layer, there are severe implications for many HF radio communication systems used at high latitudes unless corrective action is taken.

**Citation:** Ritchie, S. E., and F. Honary (2009), Storm sudden commencement and its effect on high-latitude HF communication links, *Space Weather*, 7, S06005, doi:10.1029/2008SW000461.

## 1. Introduction

[2] This paper contains two case studies that examine the significant propagation mode changes that occur immediately following storm sudden commencement (SSC) events. The studies demonstrate the effect of these changes on propagation links operating in and through the auroral zone. The key changes in the ionosphere following the onset of a disturbed ionosphere is the rapidly dwindling influence of the *F* layer as a viable reflecting layer and the rise of the *E<sub>s</sub>* layer as the primary, and in many cases, the only available reflecting layer. This change in propagation mode has implications for system design when reliable HF communications must be ensured and, focuses attention on the importance of understanding the *E<sub>s</sub>* layer so that corrective action can be taken.

[3] Sporadic *E* (*E<sub>s</sub>*) is characterized by little or no retardation at its critical frequency when viewed on an oblique ionogram, and may be either blanketing (totally reflecting)

or semitransparent (partly reflecting), up to very high frequencies. It is understood that energetic particles play a vital role in the production of *E<sub>s</sub>* and that at high latitudes the precipitation of energetic charged particles into the upper atmosphere is a regular occurrence. Most of the time at high latitudes the ionisation is dominated by energetic charged particles and only rarely is the ionosphere “quiet,” i.e., varying only with solar zenith angle and solar activity (M. Friedrich, Data coverage for D-region modelling, paper presented at XXVIIth General Assembly, International Union of Radio Science, Maastricht, Netherlands, 17–24 August, 2002). These precipitating particles, primarily kilovolt electrons produce most of their ionisation in the *E* region [Rees, 1963; Walker, 1972]. The maximum density in the disturbed dark ionosphere near 65° latitude usually occurs in the auroral *E* layer, a thick layer (relative to HF radio wavelengths) with typical electron number densities of  $2$  to  $5 \times 10^{11} \text{m}^{-3}$  extending for several degrees of latitude, i.e., a dense, thick and widespread in latitude reflecting layer. The density of the auroral *E* layer is primarily a function of the rate at which energy is deposited in the *E* region by particle

<sup>1</sup>Commission for Communications Regulation, Dublin, Ireland.

<sup>2</sup>Department of Communication Systems, University of Lancaster, Lancaster, UK.

precipitation, and has been shown to be a highly variable phenomenon [Baron, 1974].

[4] The precipitation of energetic particles is modulated considerably by geomagnetic storms and substorms. In the course of a substorm, the precipitation of the charged particles from the magnetosphere into the ionosphere takes place, the electrojet is increased, the substorm current wedge system is formed and the electron density and composition of the ionosphere is changed [Buonsanto, 1999]. It is known that during the substorm growth phase, accelerated particles from the solar wind can penetrate through the entry layer of the magnetosphere into the auroral ionosphere [Blagoveshchensky *et al.*, 2005], causing  $E_s$  layers.

[5] There have been numerous studies of the high-latitude ionosphere to aid in understanding the response of the HF communication channel to space weather effects. A review of both effects and the associated problems, with many references, is provided by Leid [1967], Goodman [1991], Davies [1991], Hunsucker and Bates [1969], and Hunsucker and Hargreaves [2003]. More recently Blagoveshchensky *et al.* [2008] examined the impact of 14 geomagnetic storms, which occurred during 1997–1999, on radio propagation conditions. In this study the variation in the delta between the monthly median values and actual maximum operation frequency (MOF) and lowest operational frequency (LOF) before, during and after storms was characterized.

[6] Several measurement campaigns covering the Arctic and relying on the oblique sounder as the primary investigating tool have been undertaken. Jull [1964] combined oblique sounder data and riometer absorption data with a view to improving the reliability of HF communications channels over and through the auroral zone during PCA events and geomagnetic storms. Owren *et al.* [1963] reported on a 3 year campaign into HF propagation over arctic paths with the behavior of multiple circuits studied in detail during disturbed periods with respect to absorption measurements and magnetic  $K$  indices. (This detailed study is also summarized by Hunsucker and Hargreaves [2003]). Goodman and Ballard [2004] reported on a 2 year campaign examining the nonclimatological patterns of signals associated with an elevated maximum observed frequency (EMOF). They describe the diurnal and seasonal behaviors of EMOF signals, the association of these observations with polar patches, blobs and the significant impact these have on over-the-pole air transport operations.

[7] Goodman *et al.* [1997] examined 28 middle- and high-latitude paths over an 18 month period to determine the value of path and frequency diversity on overcoming various deleterious effects and a practical engineering solution was offered to affect a near 100% channel availability. Bröms and Lundborg [1994] and Lundborg *et al.* [1995] reported on two oblique sounding campaigns undertaken in Sweden. The first campaign examined the variation of F2MOF, 2-hop F2MOF and LOF on short time scales from day to day outside disturbed conditions, noting the good

agreement between oblique and vertical sounder data and the linear relationship between variations in F2MOF and 2-hop F2MOF. The later campaign, covering the maximum of solar cycle 22, assessed the accuracy of prediction methods during regular and disturbed periods and the possibilities of exploiting any additional propagation modes such as backscatter, spread  $F$  and sporadic  $E$ .

[8] While the influence of  $E_s$  on high-latitude propagation has been published before [e.g., Blagoveshchensky *et al.*, 2008; Jull, 1964; Goodman *et al.*, 1997] this paper presents a comprehensive assessment of two specific links with a variety of sensors and techniques, some of which were not available until recent years. Both case studies presented in this paper use Storm Sudden Commencements as the starting point for analysis. Disturbances in the solar wind such as shock waves and dynamic pressure pulses [Wilken *et al.*, 1982; Tsurutani *et al.*, 1995; Takeuchi *et al.*, 2002], when impinging on the Earth's magnetosphere, compresses it and increases the magnetopause current. This leads to a change in the low-latitude ground-based geomagnetic field intensity, lasting typically for some tens of minutes. These signatures in the geomagnetic  $H$  field, seen suddenly and simultaneously at ground magnetic observatories [Rastogi *et al.*, 2001] are called storm sudden commencements and mark the beginning of a geomagnetic storm or an increase in activity lasting at least 1 h.

[9] These SSC are understood to be the magnetic signature of an interplanetary shockwave, for example, Burlaga and Ogilvie [1969] report that all seven SSC events in their study were caused by hydromagnetic shocks in the solar wind. The SSC generated by these hydromagnetic shock waves transform the magnetosphere into a new compressed steady state configuration which is in balance with the increased solar wind pressure [Wilken *et al.*, 1982, 1986; Tamao, 1975]. In achieving the new steady state configuration a substantial flux of energetic particles are caused to precipitate into the high-latitude ionosphere.

[10] The advantages of using SSC events as the point of origin of both case studies is twofold. First, the SSC identifies the start of the change of composition of the ionosphere with associated energetic particle precipitation. Second, the occurrence and timing of an SSC is internationally agreed [International Service of Geomagnetic Indices, 2008] and therefore a very useful reference point when comparing results from a number of different instruments in different locations.

## 2. Importance of the $E_s$ Layer for HF Communications at High Latitudes

[11] The use of HF radiocommunications at high latitudes still forms the back bone of many communications systems. At high latitudes there are few alternatives to HF radio for the merchant and fishing fleets, military forces (land, sea and air) and for the civil aviation industry. HF propagation at high latitudes during magnetic disturbances has been an enigma, in part because ionograms do not always provide analyzable data because of absorption,

blanketing and spread  $F$ . Following disturbances, rapid and large changes in ionospheric parameters occur, apparently so randomly that little sense can be made of them.

[12] Crucial to the importance of the  $E_s$  layer, is that at high latitudes the critical frequency of the  $F_2$  layer ( $f_oF_2$ ) is not much greater than the critical frequency of the  $E_s$  layer ( $f_oE_s$ ) and therefore most rays are cut off by the  $E_s$  layer, showing up as one or two hop  $E_s$  layer reflections instead of the expected one hop  $F_2$  reflection. However, these  $E_s$  modes have different frequency/ground range dependencies than the  $F_2$  mode. This phenomena known as "E layer cut off" [Davies, 1965] is significant in high-latitude regions because any frequency which penetrates the  $E_s$  layer at a given point to reach the  $F$  layer is also close to the maximum useable frequency (MUF) of the  $F_2$  layer at its point of incidence with that layer. Partially reflecting  $E_s$  can cause serious multipath and mode interference, especially detrimental to data transmission systems.

[13] A further reason for unreliable  $F_2$  mode propagation at high latitudes is the possibility of complete blockage (or screening) of the  $F$  layer by  $E_s$ . This occurs when the electron density in the  $E$  region is sufficiently enhanced so that penetration of the layer is not possible and  $E_s$  blocks propagation via higher-altitude layers. Such a layer of  $E_s$  would augment the power in a signal propagated at a frequency below the  $E$  layer MUF. For example, a highly ionised patch of  $E_s$  may make  $F_2$  layer propagation impossible but may also contribute to a low-loss reflection point on an  $E$  mode propagation path thus enhancing that mode's signal quality.

[14] While these characteristics can be helpful or harmful to radio communications, either type of  $E_s$  (i.e., partially blanketing and full blanketing) may extend the useful frequency range and its presence can be effectively used in system design and operations if it is understood [Lane, 2001]. Of course, for the  $E_s$  mode path to be successfully used, the antenna at both the receiver and transmitter must have a suitable radiation pattern with sufficient gain to take advantage of the different range of transmission angles required to achieve the same ground range as a  $F$  layer using a  $E_s$  layer reflection path.

### 3. Data and Instrumentation

[15] The primary instrument used in these case studies to demonstrate the effect of  $E_s$  layers on HF communications, immediately following an SSC event, is an oblique sounder. The University of Leicester oblique sounder system consisted of a swept frequency HF transmitter at Isfjord, Svalbard and a receiving system set up initially at the Collaborative UK Twin Located Auroral Sounding System (CUTLASS) radar site in Hankasalmi, Finland and then at Malvern, UK. The transmitter was operated by the Defense Evaluation and Research Agency (DERA), Malvern, and consists of an exciter unit developed and built by the Radio and Space Plasma Physics Group at Leicester University and a transmitter built by DERA. The unit transmits a chirp signal ranging in frequency from 2

to 30 MHz into a broadband antenna. The transmitter power is approx 10W and the sweep time is approx 5 min. The receiver consists of the DERA Iris receiving system supplemented by a communication system developed at Leicester to provide real-time control and data recovery [University of Leicester, 2007].

[16] Oblique ionograms obtained from the system indicate the modal structure of signals propagating between Svalbard and Hankasalmi and Svalbard and Malvern, at frequencies up to 30 MHz. Soundings are carried out at 15 min intervals and the results are shown as oblique ionograms. In the oblique sounder ionograms the abscissa is sounding frequency given in MHz and the ordinate axis is group delay in milliseconds. The delay indicated on the ionograms is a relative rather than absolute delay as the receiver locks onto the earliest arriving signal to set the axis.

[17] Supporting data is obtained from vertical sounders, more commonly known as ionosondes, located at Tromsø and Gakona. The basic principle of vertical incidence ionospheric sounding is that HF radio waves are reflected at the cut-off frequencies of the ionospheric magnetoplasma. To probe the  $E$  and  $F$  regions of the ionosphere a vertical sounder scans from 1 to 20 MHz, transmitting modulated radio waves and receiving and analyzing the reflected echo signals from the ionosphere [Wright *et al.*, 1957; Piggott and Rawer, 1972]. Conventionally the ionosonde presents the demodulated echo signals as time of flight (range) versus sounding frequency in the form of ionograms. Extensive details on ionosondes and their applications are given by Ivanov *et al.* [2003] and Reinisch [1996].

[18] Electron densities in the  $E$  and  $F$  regions are obtained from incoherent scatter radars (ISR), namely the European Incoherent Scatter (EISCAT) UHF radar near Tromsø and the Incoherent Scatter Radar (ISR) at Sondrestrom, Greenland. In the ISR method, incoherent scatter is produced by backscatter from the thermal irregularities in the ionization in the upper atmosphere. The signal amplitude and spectral shape yield the electron density and electron and ion temperature, while the spectral shift yields the average velocity of the ions [Bates and Hunsucker, 1974].

[19] Solar Wind and interplanetary magnetic field (IMF) data is obtained from measurements taken by the Advanced Composition Explorer (ACE) spacecraft. The ACE satellite carries high-resolution sensors and monitoring instruments that sample the parameters of low-energy particles of solar origin and high-energy galactic particles. See Stone *et al.* [1998] for comprehensive details of the satellite and instrumentation.

[20] Magnetometer data was collected from the Glenmore Lodge magnetometer which is part of SAMNET, the UK Sub-Auroral Magnetometer Network which continuously records natural variations in the Earth's magnetic field giving information about the complex interactions within the coupled Solar Wind-Magnetosphere-Ionosphere sys-

**Table 1.** Instrument Location Details

Instrument	Location	Code	Latitude	Longitude
Oblique Sounder Transmitter	Svalbard	A	78.21 N	15.63 E
Oblique Sounder Receiver	Hankasalmi	B	62.32 N	26.61 E
Oblique Sounder Receiver	Malvern	C	52.10 N	2.32 W
Vertical Ionosonde	Tromso	D	69.60 N	19.20 E
Vertical Ionosonde	Gakona	F	62.12 N	214.86 E
ISR (EISCAT)	Tromso	G	69.58 N	19.23 E
ISR	Sondrestrom	H	66.99 N	309.05 E
Magnetometer	Glenmore Lodge	I	57.16 N	3.68 W
Riometer	Kilpisjärvi	J	69.10 N	20.80 E
Advanced Composition Explorer Satellite	L1 Libration Point			

[21] Riometer data was obtained from the Imaging Riometer for Ionospheric Studies (IRIS) located at Kilpisjärvi, Finland. In essence a riometer observes temporal variations in ionisation in the *D* and *E* regions caused by charged particle precipitation [Hargreaves, 1969]. While the most common form of riometer uses a wide beam antenna with bandwidths of in the order of 60° [e.g., Little and Leinbach, 1959], the IRIS has 49 narrow beams of beam width between 13° and 16° [Browne et al., 1995] and operates as a fast-scan multiple beam instrument which examines the whole ionospheric sky to 45° from zenith. Operation is passive and the background cosmic radio noise from the sky is constantly monitored. By comparing the background cosmic radio noise from the sky against the received signal for an undisturbed day it is possible to determine the variation of ionospheric absorption within each beam.

tem. Each station records the magnetic field in three orthogonal components: *H*, *D*, and *Z*, these being horizontal magnetic northward, horizontal magnetic eastward and vertically downward.

[22] Table 1 details the location of all instruments used in these studies which are shown in Figure 1, on a great circle map centered on the oblique sounder transmitter at Svalbard

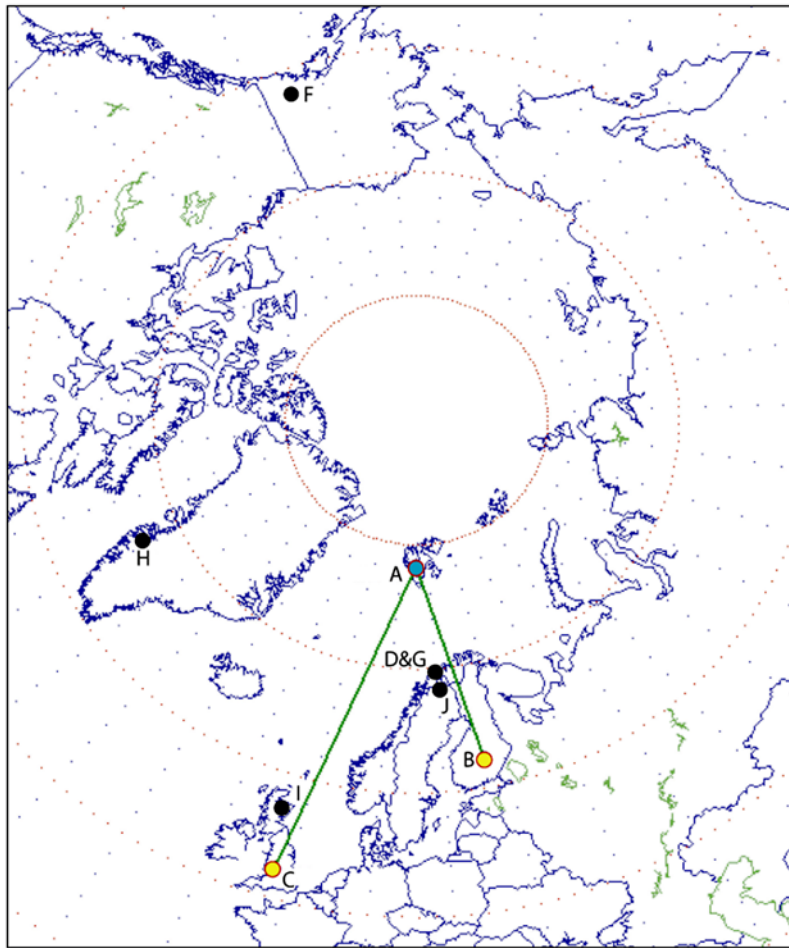


**Figure 1.** Great circle map centered on the oblique sounder transmitter at Svalbard showing the locations of all the instruments mentioned. Alphabetic codes indicate the instrument as listed in Table 1.

**Table 2.** Bearing and Distance Information for Both Great Circle Propagation Paths

Path	Bearing (deg)	Distance (km)
Great circle propagation path from A to B	161.6	1807
Great circle propagation path from A to C	204.7	2990

Svalbard. Table 2 details the bearing and range of the great circle propagation path between the oblique sounder transmitter and both oblique sounder receiver sites shown in Figure 1.

#### 4. Case Studies

[23] The case studies presented in this paper examine two north-south auroral propagation paths following the onset of a geomagnetic disturbance. The objective of these studies is to understand the changes that occur in the ionospheric layers and the resultant propagation mode changes that occur. This will reveal how propagation modeling needs to adapt in order to best utilize the changes that occur as well as the practical aspects that must be considered when using the modified ionosphere.

[24] The key difference in the two case studies is the great circle path length between the transmitter and the receiver. In the first case study with a path length of 1807 km the 1E mode of propagation dominates following the SSC. In the second case study, with a path length of nearly 3000 km, the 2E mode of propagation dominates.

##### 4.1. SSC of 31 July 1999

[25] This case study examines the propagation path between Isfjord, Svalbard and Hankasalmi, Finland a distance of 1807 km following an SSC at 1827 UT on 31 July 1999.

[26] In the period preceding 31 July 1999 solar activity ranged from low to high levels [NOAA, 1999a]. Solar activity increased to high levels on 29 July by virtue of an impulsive M5 flare on the 29 July at 19:34UT from Region 8651 which was accompanied by minor discrete radio emissions. Activity returned to moderate levels on 30 July with another isolated, low-level M class flare from Region 8649. A coronal mass ejection signature was evident on 30 July with a velocity increase from 380 to 680 km s<sup>-1</sup>, increased densities, and a period of sustained southward IMF  $B_z$  with deflections to minus 12 nT (GSM). Activity decreased to low levels on the day following the SSC with occasional C class flares from regions 8645 and 8651. No proton events were detected at geosynchronous orbit during the period. The solar wind and IMF data for the immediate period of the SSC is shown in Figures 2a–2d.

[27] Figure 2a represents the solar wind particle density (cm<sup>-3</sup>) against time. At 1740 UT following 7 h of low activity and low density (1.37 cm<sup>-3</sup>) the density increases very quickly to 11.4 cm<sup>-3</sup>. The density remains at elevated

levels for more than 1 h before moderating. Figure 2c represents  $B_z$ , the north-south component of the IMF.  $B_z$  is positive when, in parallel with the Earth's field, the northward direction of the magnetic field points upward. At the magnetopause the Earth's magnetic field and the IMF come into contact. If the IMF points southward (i.e.,  $B_z$  is negative) then the IMF can partially cancel the Earth's magnetic field at the point of contact, make direct connection with field lines and allow the injection of energy into the magnetosphere. Southward turning of the IMF initiates changes in the configuration of the magnetosphere, Earthward displacement of the magnetopause and tailward stretching of the field lines, where energetic particles are more subject to precipitation because of changes in drift shells [Ranta and Ranta, 1990].

[28] From 1000 to 1530 UT  $B_z$  is mainly northward with a few short excursions southward. Just before 1530 UT  $B_z$  becomes predominantly southward with an excursion northward around 1600 UT. Coinciding with the sudden increase in density (Figure 2a) at 1740 UT is a sudden change in the direction of  $B_z$  from south to north.  $B_z$  turns southward again after 2 h of maintaining its northward direction. Figure 2b represents the solar wind particle velocity (km s<sup>-1</sup>) and shows an increasing velocity coinciding with the increase in particle density, IMF field strength and the change in  $B_z$ . The values of solar wind particle density and velocity have a direct and strong correlation to the amplitude of the IMF which in turn influences the location of the magnetopause [Fairfield, 1971].

[29] These sudden enhancements in the solar wind dynamic pressure are known to compress the magnetosphere and enhance the magnetopause current [Kaufmann and Konradi, 1969], as well as the tail currents [Russell et al., 1994]. Zesta et al. [2000] noted in a study of the 10 January 1977 disturbance that the response of the magnetosphere to a pressure front was practically instantaneous, global and directly driven by the propagation of the solar wind density enhancement region through the magnetosphere. The disturbance is transmitted throughout the magnetosphere in the form of hydromagnetic waves and has been observed both at satellite altitudes and on the ground as a sudden increase or decrease in the geomagnetic field strength. Corresponding to the changes in geomagnetic field strength are changes in the magnetic field geometry, the electric field configuration as well as changes in thermal and energetic particle distributions.

[30] The geomagnetic field was at quiet to unsettled levels until 31 July when a sudden storm commencement occurred at 1827 UT followed by active to major storm levels with brief severe storm periods at high latitudes. The disturbance continued until 1 August (not shown here). Magnetometer data for the immediate period of the SSC is shown in Figure 2e. It can be seen that the disturbance in the solar wind measured at the ACE satellite at 1740 UT took circa 45 min to reach the magnetosphere and for the effect to be measured by the

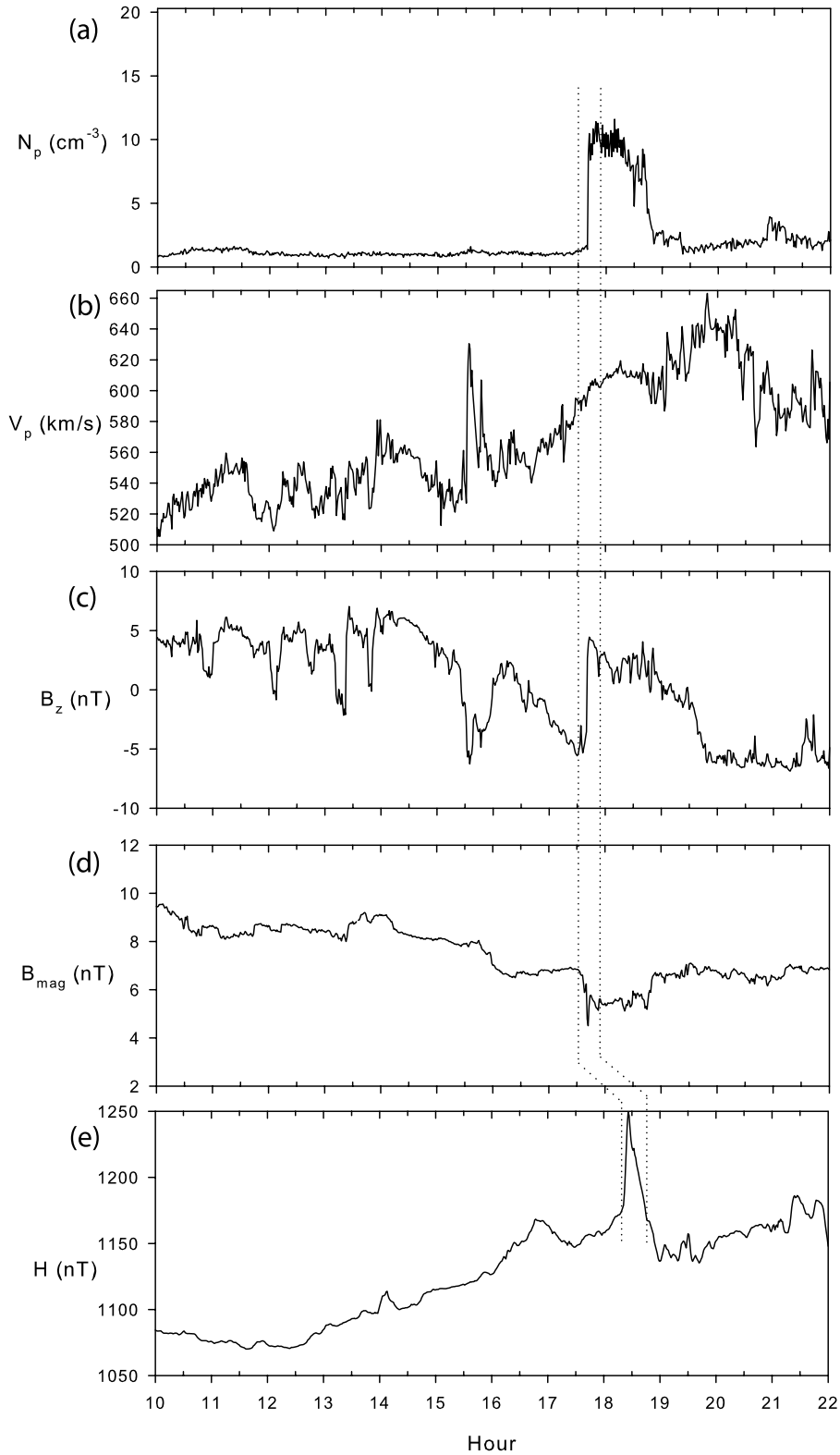


**Figure 2.** Solar Wind and IMF data from the ACE satellite for the first case study is shown, namely, (a) plasma density, (b) speed, (c) the  $B_z$  magnetic component, and (d) total field strength. (e) Magnetometer data (the horizontal intensity ( $H$ ) component) is shown. Dashed lines indicate the period of disturbance.

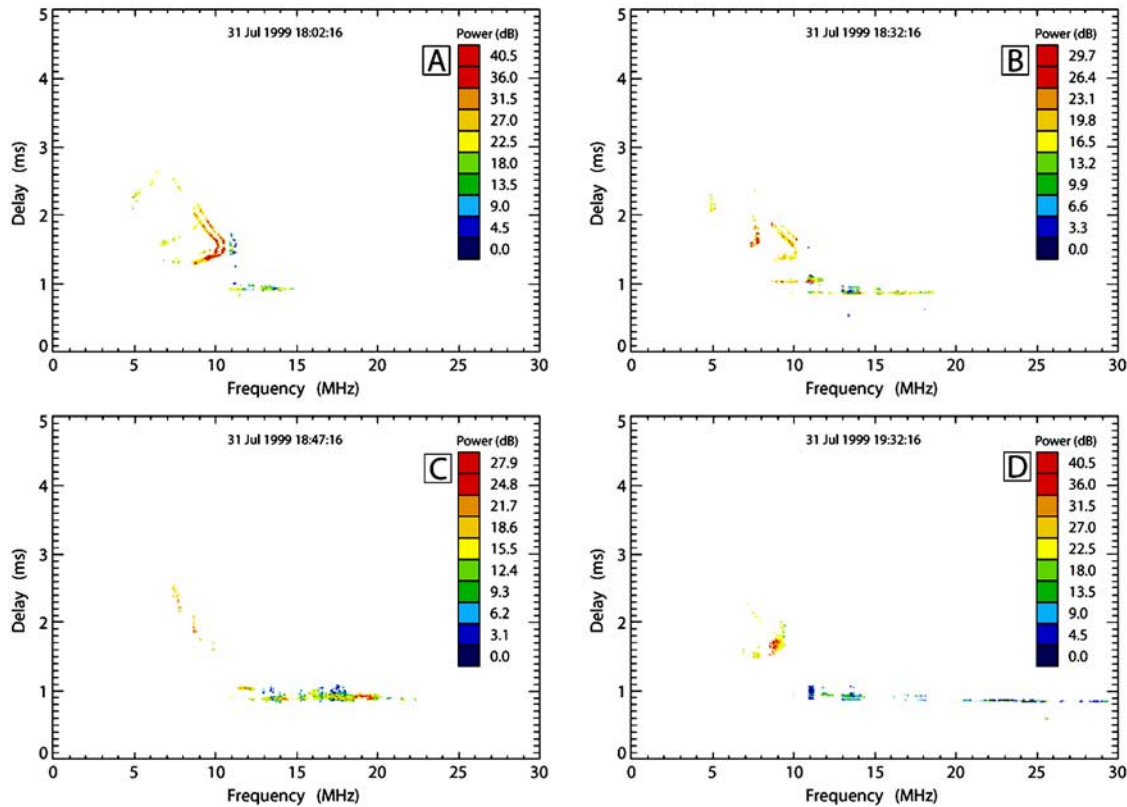


Figure 3. Selection of oblique ionograms from the Svalbard to Hankasalmi path.

Glenmore Lodge magnetometer at 1825 UT where the  $H$  component increased from 1171 nT to a peak of 1249 nT over a period of 6 min.

[31] Figure 3 is a selection of oblique sounder ionograms covering the period from 25 min before to 60 min after the SSC occurred. Twenty-five min before the SSC occurred the ionosphere is fairly quiet as the oblique ionogram in Figure 3a reflects. Figure 3a shows reflections from 8 to 11 MHz from the  $F$  layer and at the incident angle required to achieve a one hop  $F$  layer path between transmitter and receiver the  $F$  layer oblique critical frequency is approximately 11 MHz. At lower-takeoff angles the  $E_s$  layer becomes usable for signals between 11 and 15 MHz along this path.

[32] Figure 3b captures the situation 5 min after the SSC occurs when particle precipitation and the resultant enhanced  $E$  layer ionisation has set in. While the  $F$  layer still provides a valid path, the enhanced electron density due to precipitation has increased the usable frequency of the  $E$  layer well above the initial value to 15 MHz. Between 9 and 10 MHz there are now two raypaths in existence, one from the  $F$  layer and a new path from the  $E_s$  layer.

[33] Figure 3c is 20 min after the SSC when the  $E_s$  layer is enhanced further as evidenced by the higher-power returns, the useful frequency of the  $E_s$  layer is further extended to more than 20 MHz. The  $F$  layer path has degraded because of intense  $D$  region absorption attenu-

ating the lower frequencies, as will be seen in Figure 4. Figure 3d is 1 h after the SSC occurs the  $F$  layer is starting to recover with a critical frequency of 9 MHz and the  $E$  layer enhancement, while patchy and a much weaker path than the  $F$  layer path, can now support frequencies up to 30 MHz.

[34] Figure 4 captures the absorption measured by beam nine of the Kilpisjärvi riometer. For this study the riometer is not ideally located to measure absorption at the exact point where the ray penetrates the  $D$  layer and is only used to illustrate the general pattern of  $D$  layer absorption in the area.

[35] Before the SSC at 18:27UT the absorption measured at 38.2 MHz is less than 0.1 dB. Following the SSC the absorption increases and at 18:47UT (Figure 3c) the absorption has increased to 0.4 dB. Neglecting the effects of the Earth's magnetic field, auroral absorption can be shown to be inversely proportional to the square of the operating frequency [Browne *et al.*, 1995], therefore 0.4 dB of absorption measured on the riometer at 38.2 MHz equates to 23 dB absorption at 5 MHz and to 6 dB at 10 MHz. Of course any ray reflecting in the ionosphere at the mid point would suffer twice this absorption as the ray penetrates the  $D$  layer twice. At 19:32UT (Figure 3d) the absorption has reduced slightly to 0.3 dB and continues to fall until 2002 UT (Figure 5a) before increasing again (as reflected in Figure 5b) at 2032 UT to values in excess of

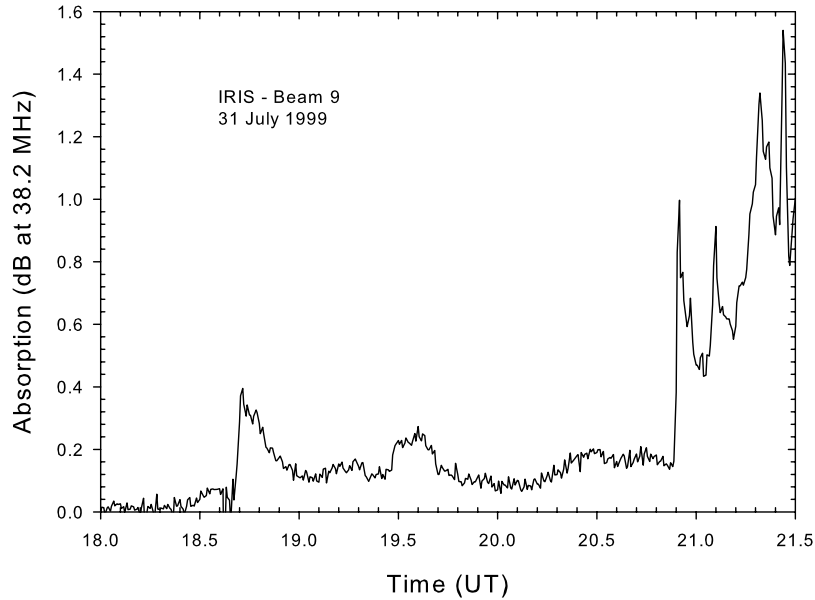


Figure 4. Riometer data from the Kilpisjärvi riometer, absorption data is from beam 25, the center beam in the array.

1 dB absorption (measured at 38.2 MHz) which equates to 58 dB absorption at 5 MHz and 15 dB at 10 MHz.

[36] Figure 5 is a further selection of post-SSC oblique ionograms. Figure 5a is 90 min after the SSC the *F* layer has recovered and assuming more of an early evening structure. *D* layer absorption has reduced sufficiently (as shown in Figure 4) so that frequencies as low as 3 MHz can be seen reflecting from the *F* layer. The *E<sub>s</sub>* layer continues to be enhanced by precipitation and maintains an oblique top frequency near 30 MHz. Figure 5b is 120 min after the SSC the *E* layer enhancement, while still significant, has begun to wane and has become patchy in places. Reflections from the *F* layer are again affected by *D* layer absorption which as shown in Figure 4 has increased at this time.

[37] Figure 6 is a selection of ionograms from the Tromso Ionosonde located approximately at the midpoint of the propagation path. Figure 6a is 4 min before the SSC occurs the ionosphere is quiet and a fairly typical early evening ionogram is displayed. The *F<sub>2</sub>* layer vertical critical frequency ( $f_oF_2$ ) is 5.5 MHz and the virtual height of the *F<sub>2</sub>* layer ( $h'f$ ) is 300 km. The *E* layer vertical critical frequency ( $f_oE$ ) is 2.85 MHz and the virtual height of the *E* layer ( $h'E$ ) is 105 km.

[38] Figure 6b is 20 min after the SSC  $f_oF_2$  remains at 5.5 MHz but  $h'f$  has increased to 385 km. The *F* layer has increased considerably in height because of electron density depletion at lower altitudes. There is some trace spread (typical of precipitation events) which makes the virtual heights difficult to determine accurately. The *E<sub>s</sub>*

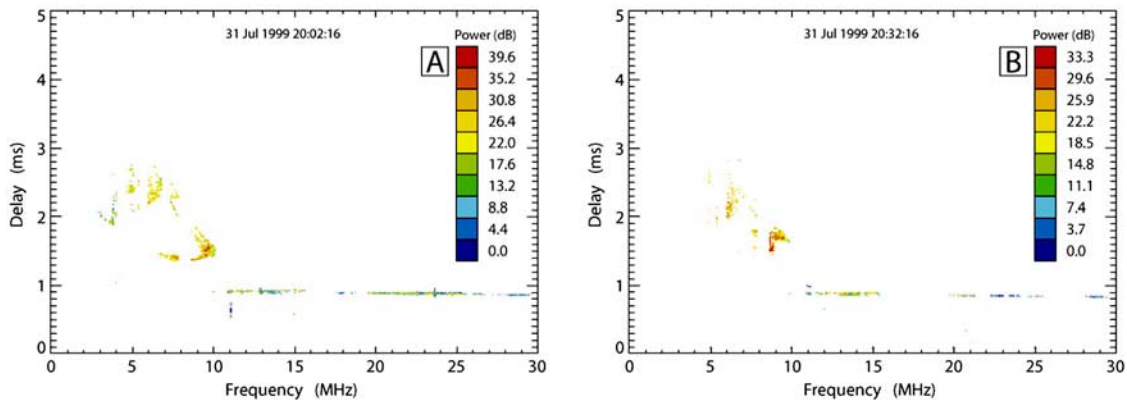
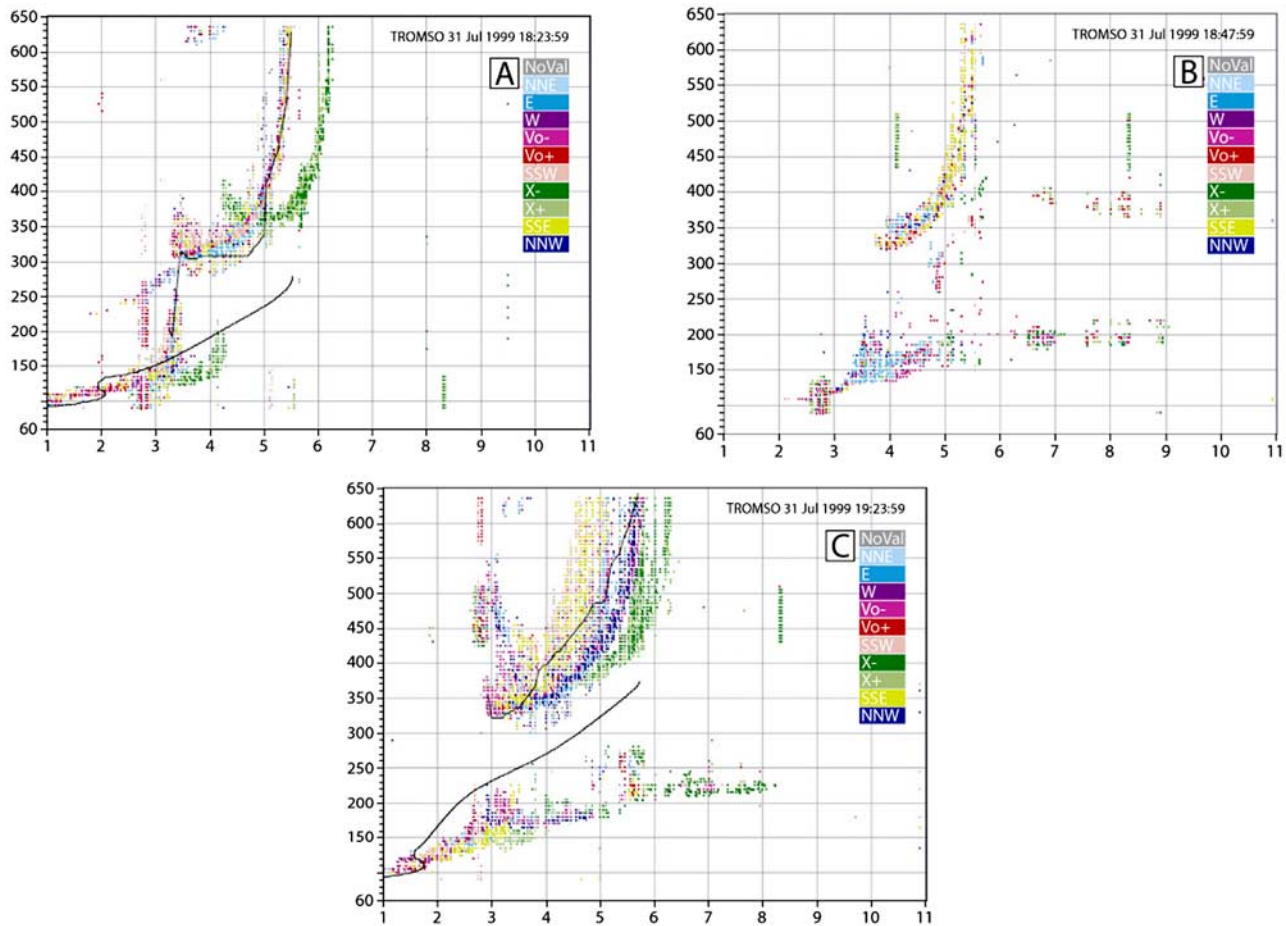


Figure 5. A further selection of oblique ionograms from the Svalbard to Hankasalmi path.



**Figure 6.** Selection of vertical ionograms from the Tromsø ionosonde. (The x axis is frequency in MHz, and the y axis is virtual height in km.)

layer has formed and  $f_oE_s$  is 4.9 MHz. The absence of any reflections below 2.5 MHz in Figure 6b is most likely due to the spike of absorption seen in Figure 4 at this time. The 0.37 dB of absorption at 38.2 MHz equates to a total absorption of 260 dB at 2 MHz for a ray passing twice through the D region.

[39] Figure 6c is 60 min after the SSC particle precipitation continues to be in evidence as shown by the widespread occurrence of spread E and spread F. The E layer has taken on a slant characteristic rising from 90 to 220 km as the frequency increases. The  $F_2$  critical frequency ( $f_oF_2$ ) is now 5.7 MHz and  $f_oE_s$  is 7 MHz (ignore the extraordinary wave reflection (green trace)). This ionogram falls just before the third absorption spike seen in Figure 4 and reflections are visible down to the lowest usable ionosonde frequency.

[40] Figure 7a is 2 h after the SSC the ionosphere has recovered with a blanketing  $E_s$  layer up to 3.3 MHz. The virtual height of the F layer has reduced slightly. Figure 7b is 3 h and 20 min after the SSC the ionosphere is further disturbed by substorms (as evident in Figure 4) which provides further precipitation of high-energy particles

resulting in the E layer reforming with  $f_oE_s$  approaching 3.5 MHz and the F layer virtual height rising to 450 km.

[41] To assist in demonstrating the problem a simple ray trace analysis of the path between Svalbard and Hankasalmi has been undertaken. The geometry of conventional mode configurations is shown in Figure 8. Symmetrical mode geometry is assumed and the location of the Tromsø ionosonde and the Kilpisjärvi riometer is indicated in relation to the distances from the transmitter.

[42] In the conventional mode and assuming an E layer height of 110 km a 1E raypath is possible with a take off angle of  $2.8^\circ$ . A 2E is also possible with a take off angle of  $11^\circ$ . Three F layer modes are possible with a 1F at  $11^\circ$ , a 2F at  $26.5^\circ$  and a 3F at  $38.5^\circ$ . The 1E and 1F control points and the second 3F control point is very nearly directly above the Tromsø ionosonde. Figure 8 shows the option for two E layer paths and three F layer paths. Evident on the oblique sounder is however only the 1E and 1F raypaths which according to Figure 8 have a reflection point in the center of the great circle path. The reflection point for any other raypaths would require similar ionospheric characteristics at each of the reflection points. For the 2E and 2F

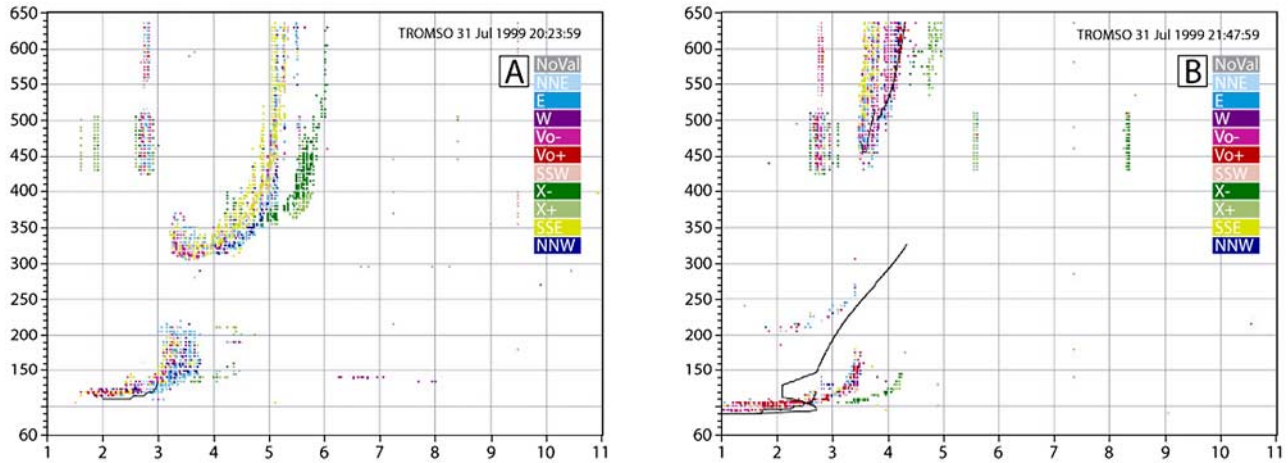


Figure 7. A further selection of vertical ionograms from the Tromso ionosonde. (The x axis is frequency in MHz, and the y axis is virtual height in km.)

paths similar ionospheric characteristics are needed at the 450 km and 1350 km reflection points. For the 3E and 3F paths, similar ionospheric characteristics would be required at the 300 km, 900 km and 1500 km reflection points. In highly variable high-latitude ionosphere it is not surprising that the conditions for any path other than the single ionospheric reflection paths (the 1E and 1F paths) is achievable. With the availability of the Tromso ionosonde close to the center of the link path, the actual virtual heights of the E and F layers can be incorporated into the geometry of the mode configurations.

[43] As shown in Figure 9 while the  $E_s$  layer modes of operation continue to operate around the 110–120 km altitude mark the convention of ray tracing the F layer at 250 km is not valid and a virtual height of 350 km is for this situation a more accurate parameter. At a F layer height of 350 km the 1F ray angle changes from  $11^\circ$  to  $14^\circ$ , the 2F

changes from  $26^\circ$  to  $35^\circ$  and the 3F ray from  $38^\circ$  to  $47^\circ$ . Figure 7b shows that the virtual height of the F layer can be as high as 450 km. With reference to Figure 9, this would require a 1F ray takeoff angle of  $22^\circ$ , a 2F takeoff angle of  $42^\circ$  and a 3F take off angle of  $59^\circ$ . In the 450 km case and in some of the 350 km case, taking the secant rule into account, it is very likely that the 2F and 3F rays are penetrating through the ionosphere and hence not reflecting in any manner.

[44] Using the modified geometry the F layer path and the  $E_s$  layer path were modeled using the well known HF propagation planning tool, VOACAP [Lane, 2001] in the point-to-point configuration. The validity of using HF propagation prediction programs has been addressed by Bröms and Lundborg [1994] who found good agreement between the prediction and measurements made during quiet conditions and Hunsucker [1999] (as summarized by

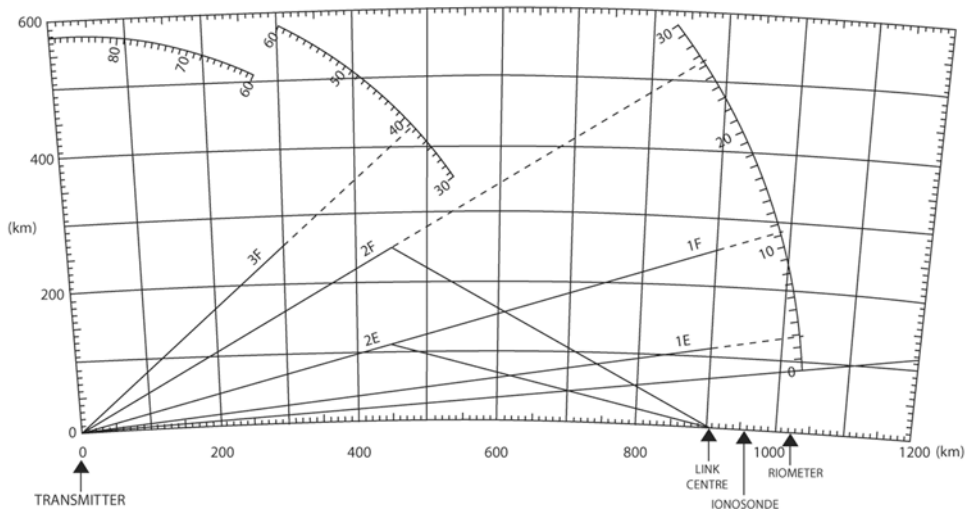


Figure 8. Geometry of conventional mode configurations.

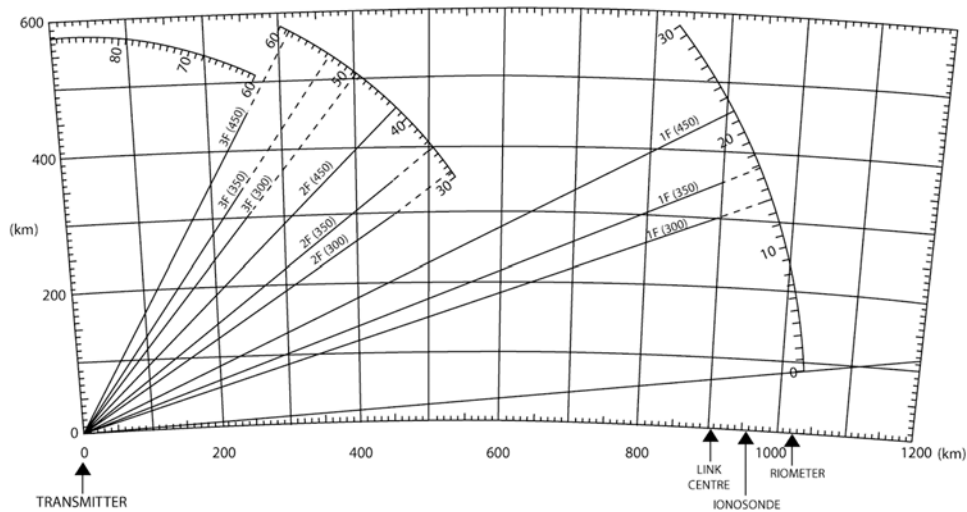


Figure 9. Modified geometry of conventional mode configurations.

Hunsucker and Hargreaves [2003]) who noted the aggregate correct prediction of these programs was only  $\sim 45\%$  under disturbed conditions. However, using the actual layer height info from the vertical sounder allows some limited but relevant modeling to be undertaken even after the onset of disturbed conditions. The modeling shows that the increase in virtual height of the  $F$  layer from 250 km to 450 km results in an increase in transmission loss of 6 dB and an additional spreading loss of 4 dB. As the  $E_s$  layer maintains its virtual height it does not suffer the same degradation. The result, for this case study, is a 10 dB increase in losses when using the partially blocked  $F$  layer during the disturbed period. In terms of signal-to-noise ratio (SNR) this results in the SNR of the  $E_s$  layer path exceeding the  $F$  layer SNR by 3–5 dB.

[45] Using 10 MHz as the default frequency of operation, the median SNR of a blanketing  $E_s$  layer increased by 3 dB over the normal (nondisturbed)  $F$  layer and increasing the frequency of operation by 3 MHz increased the median SNR achievable on the link by 8 dB overall and the increase in SNR has a direct affect on the reliability of the link. The principle being demonstrated is that a small increase in operating frequency during the disturbed period can assist in maximum utilization of a blanketing  $E_s$  layer.

[46] The apparent increase in received field strength is not clearly shown in the oblique ionograms. This is most likely as a result of the antenna used at both the transmitter and receiver sites. The radiation angle of the vertical antenna varies considerably as operating frequency varies [McNamara, 1991] and with the wide operating range of the oblique sounder (2 – 30 MHz) it is very difficult to achieve sufficient gain at low-elevation angles, less than  $3^\circ$  in this case study. As a result the oblique ionograms do not reflect the increase in SNR in the  $E_s$  layer returns when compared to  $F$  layer returns for which the vertical dipole antenna is better matched. The princi-

ple that must be taken into account if the  $E_s$  layer is to be used as a replacement for the  $F$  layer during disturbed periods is that an antenna capable of fully utilizing the very low elevation angles must be used. A further practical consideration in very low angle operations is the need to clear any obstruction at the receiver and transmitter site to maximize this mode of operation. The very low angles in use do however restrict the lengths of any  $1E_s$  path to an absolute maximum of 2000 km after which the takeoff angle is reduced to nearly  $0^\circ$ .

#### 4.2. SSC of 15 September 1999

[47] This further example examines the propagation path between Isfjord, Svalbard and Malvern, UK a distance of 2990 km. This case study is different from the first in a number of ways. First the great circle path length is long enough to preclude a  $1E$  mode of propagation and the receiver is well out of the auroral zone. The  $B_z$  component of the solar wind does not change direction following the evening SSC being northward before the SSC at 2019 UT and moving further northward in the 5 h following the SSC. There is a greater delta change in  $f_oE$  immediately following the SSC followed by similar subsequent changes to the value of  $f_oE$ . Finally, ISR data is available from two spatially well separated instruments showing the changes in electron density in the ionosphere before and after the SSC occurs.

[48] Solar activity was predominately low before and after 15 September dominated by events in Region 8700 which developed a mixed polarity sunspot group and produced numerous C class flares [NOAA, 1999b]. The period before and after 15 September was dominated by high-speed coronal hole conditions. Wind speeds were high, ranging from 550 to 650 km  $s^{-1}$  and the IMF  $B_z$  fluctuated between northward and southward for most of the time with prolonged periods of predominately southward conditions. No proton events were detected at geo-

synchronous orbit during the period. The solar wind data for the immediate period of the SSC is shown in Figures 10a–10d.

[49] Figure 10a shows solar wind particle density ( $\text{cm}^{-3}$ ) against time. The first disturbance occurred at 0703 UT when the density increased from  $2.9 \text{ cm}^{-3}$  to a peak of  $6.6 \text{ cm}^{-3}$ . The second clearer step change occurred at 19:41UT when the density suddenly increased from  $2.8 \text{ cm}^{-3}$  to  $7.5 \text{ cm}^{-3}$ . In both cases there was more than a doubling of density. Figure 10b shows the solar wind particle velocity, at the first disturbance the velocity increased from  $486$  to  $605 \text{ km s}^{-1}$  a substantial change of more than  $100 \text{ km s}^{-1}$ . At the second disturbance the velocity increased from  $560$  to  $608 \text{ km s}^{-1}$ , an increase of  $48 \text{ km s}^{-1}$ .

[50] Figure 10c shows the magnitude and direction of  $B_z$ ,  $B_z$  is slightly southward and moves slightly northward just before the first disturbance and becomes stronger southward following the disturbance. The situation is different for the second disturbance as  $B_z$  has been northward for a number of hours before the disturbance and becomes even stronger northward following the disturbance. Figure 10d shows the interplanetary magnetic field strength (nT). The magnetic field strength jumps from  $6 \text{ nT}$  to  $12.1 \text{ nT}$  during the first disturbance and from  $4.7 \text{ nT}$  to  $8.3 \text{ nT}$  during the second disturbance.

[51] The geomagnetic field experienced minor to major disturbances at high latitudes associated with a high-speed coronal hole stream over the week 13 – 19 September 1999. On September 15 midlatitudes experienced minor storm level and high latitudes experienced severe storming in conjunction with the high-speed shock mentioned above. The effects of the high-speed stream began to diminish only four days later. Magnetometer data for the immediate period of the SSC is shown in Figure 10e. The first disturbance in the solar wind at 07:03UT was measured on the Earth's surface at 07:55UT. The magnetometer displayed a small reduction in the H component, a recovery and then a step decline from  $1108 \text{ nT}$  to  $1045 \text{ nT}$ . The second disturbance in the solar wind at 19:41UT was measured by a change in the magnetometer from  $1128 \text{ nT}$  to a peak of  $1156 \text{ nT}$  at 2020 UT. Both magnetometer signatures are typical mid- to high-latitude magnetometer SSC indicators with preliminary and main impulses as explained by *Ferraro et al.* [1951] and *Araki* [1977].

[52] The UHF ISR at Tromso was in operation from 15:08 on 15 September 1999 to 13:00 the following day. Figure 11 shows the electron density versus altitude data from 1508 UT on the 15 September until noon on the next day. When the ISR begins measurements the *E* region electron density above  $100 \text{ km}$  altitude is already enhanced because of magnetic activity during the day following the 0753 UT SSC.

[53] At the time of the second SSC (2019 UT) the ISR shows a sudden enhancement in electron density at altitudes around  $150 \text{ km}$  and low as  $100 \text{ km}$ . The electron density increases from about  $2.5 \times 10^{10} \text{ m}^{-3}$  to  $6.3 \times$

$10^{10} \text{ m}^{-3}$ , more than a doubling of electron density which lasts for more than 3 h. It should be noted that the electron density values quoted should not be seen as absolute values but rather as an indication of the scale of change that occurs during this period and the subsequent effect on ionospheric propagation. The electron density between  $100 \text{ km}$  and  $150 \text{ km}$  altitude decreases after midnight but just after 0100 UT the following day the electron density undergoes frequent and intense enhancements until at least 1100 UT. This is a result of ongoing precipitation due to substorms that followed the SSC.

[54] Figure 12 covering the same period as Figure 11 is taken from the ISR at Sondrestrom which was in operation from 2241 UT on 14 September to 2400 UT on 17 September 1999. The *E* region enhancement (circled in Figure 12) begins near 20:20UT and lasts for about 2 h, very similar to what has been seen in the EISCAT data even though the two ISR's are spatially well separated (Figure 1 refers). Following a 3 h period of relative quiet the Sondrestrom ISR shows a 2 h sudden enhancement in electron density reaching peaks of  $13 \times 10^{10} \text{ m}^{-3}$ . Again the electron density values quoted should not be seen as absolute values but rather a reflection of the scale of change that is possible and the consequences these changes have on ionospheric propagation.

[55] A selection of oblique sounder ionograms from the Svalbard to Malvern propagation path are shown in Figure 13. Figure 13a is 17 min before the SSC occurs the *F* region is disturbed with only a small window of reflection between  $2.5 - 4 \text{ MHz}$ . There is a slight return from the *E* layer around  $11 \text{ MHz}$ . Figure 13b is 13 min after the SSC occurs the high-latitude *E* region is strongly enhanced forming an  $E_s$  layer reflection path between  $10$  and  $18 \text{ MHz}$ . At this point there is virtually no *F* layer path visible.

[56] Figure 13c is a further 60 min on and the situation remains unchanged. Standard predictions of this propagation path are useless as the enhanced *E* region dominates and no *F* layer path is available. Figure 13d is a further 60 min on, now 2 h and 15 min after the SSC occurs and the situation remains virtually unchanged. The *E* region window has reduced slightly to cover  $10.8 - 17.5 \text{ MHz}$ . There is a slight return from the *F* layer around  $2 \text{ MHz}$ . It is likely that any return of signals below  $10 \text{ MHz}$  is either suffering extensive *D* region absorption or there is simply no suitable reflecting *F* layer available because of ionisation depletion at these altitudes.

[57] Figure 14 is a selection of ionograms from the Tromso Ionosonde showing similar characteristics to that seen in the first case study. Figure 14a is 7 min before the SSC occurs. The *F* region is disturbed and  $h'F$  has already increased to  $405 \text{ km}$ . This change in reflection height would adversely affect HF links and HF broadcasting services which usually assume an  $h'F$  of around  $250 \text{ km}$  in the planning process which in turn determines the amount of power and type of antenna to be used. The antenna type is most often dependent on the takeoff angle

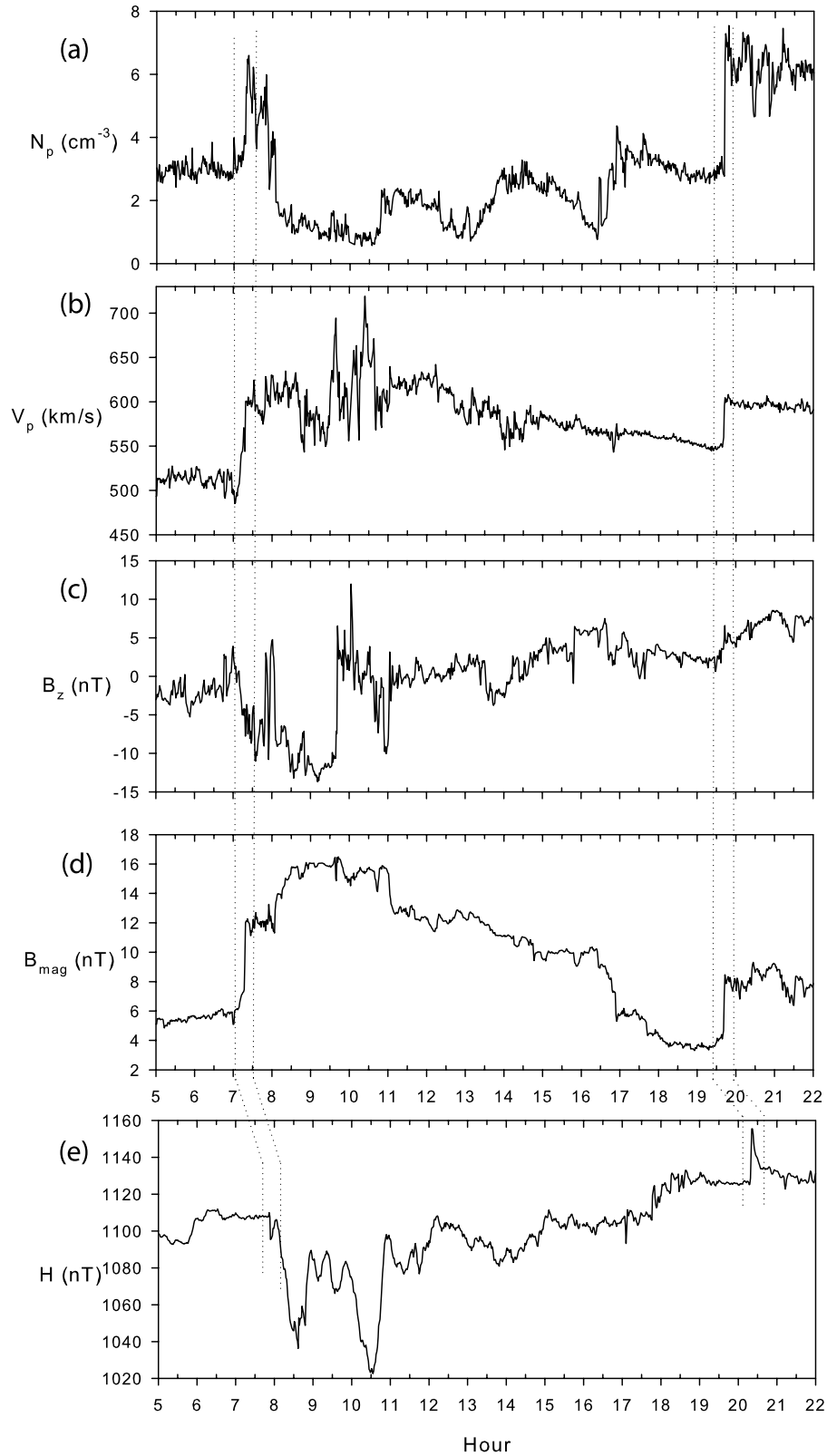


**Figure 10.** Solar Wind data from the ACE satellite for the second case study is shown, namely, (a) plasma density, (b) speed, (c)  $B_z$ , and (d) total magnetic field. (e) Magnetometer data (horizontal intensity ( $H$ ) component) is shown. The dashed lines delineate the two periods of SSC disturbance.

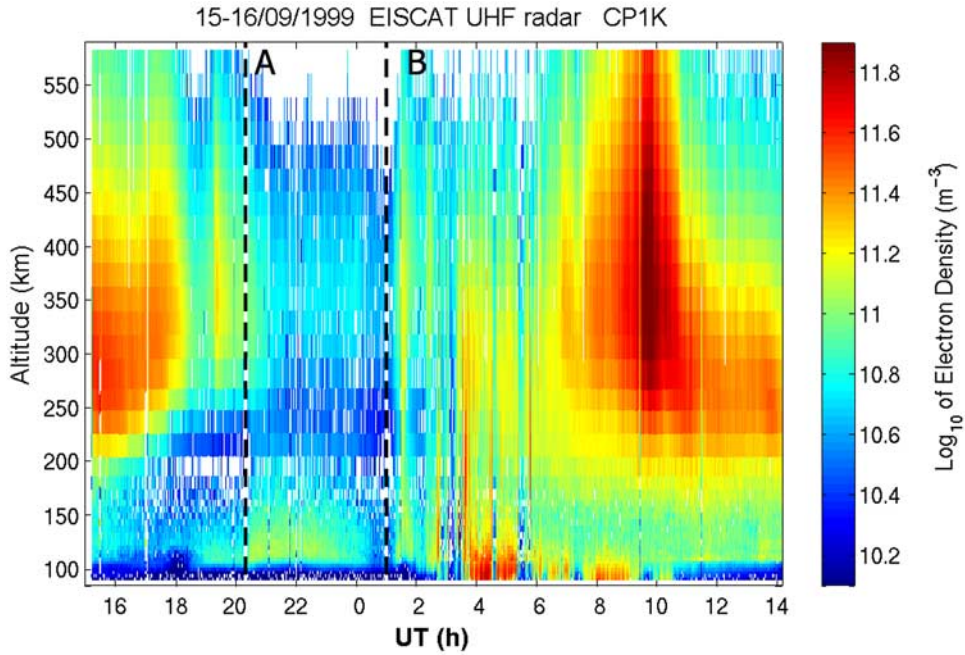


Figure 11. EISCAT UHF incoherent scatter (IS) radar captures the changes in electron density from 1508 UT on 15 September 1999 till after noon the following day. Dashed line A marks the moment of SSC, and dashed line B marks the onset of frequent and intense substorms.

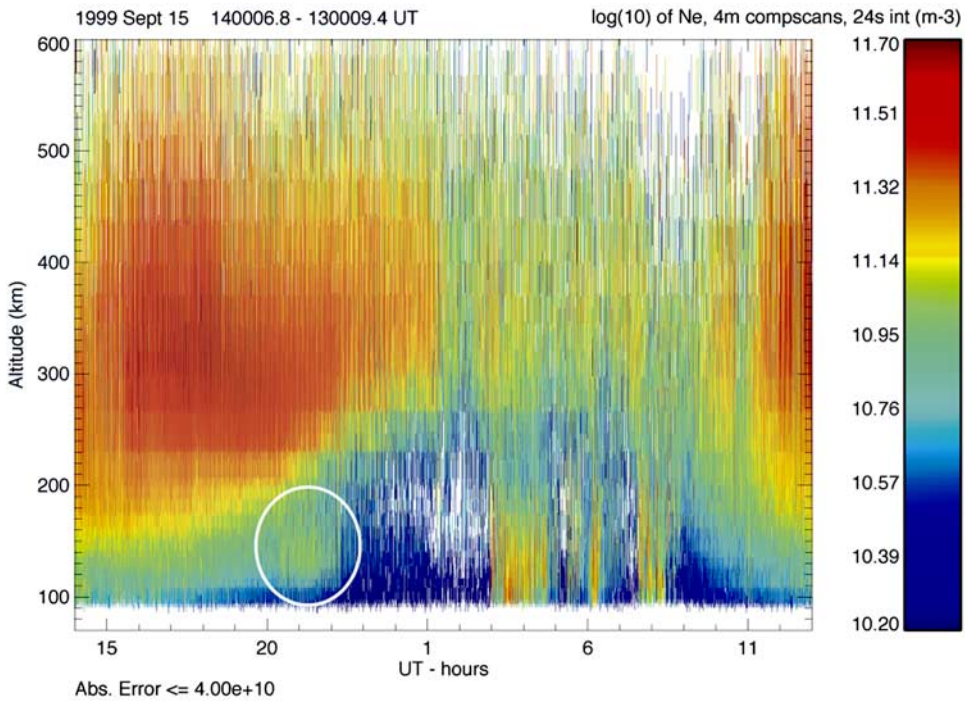


Figure 12. Sondrestrom IS radar captures the changes in electron density at 130 km altitude. The circle indicates the enhancement of Ne at E layer altitude at the time of SSC. Note the onset of substorm activity from 0300 UT the following morning causing further enhancements to electron density.

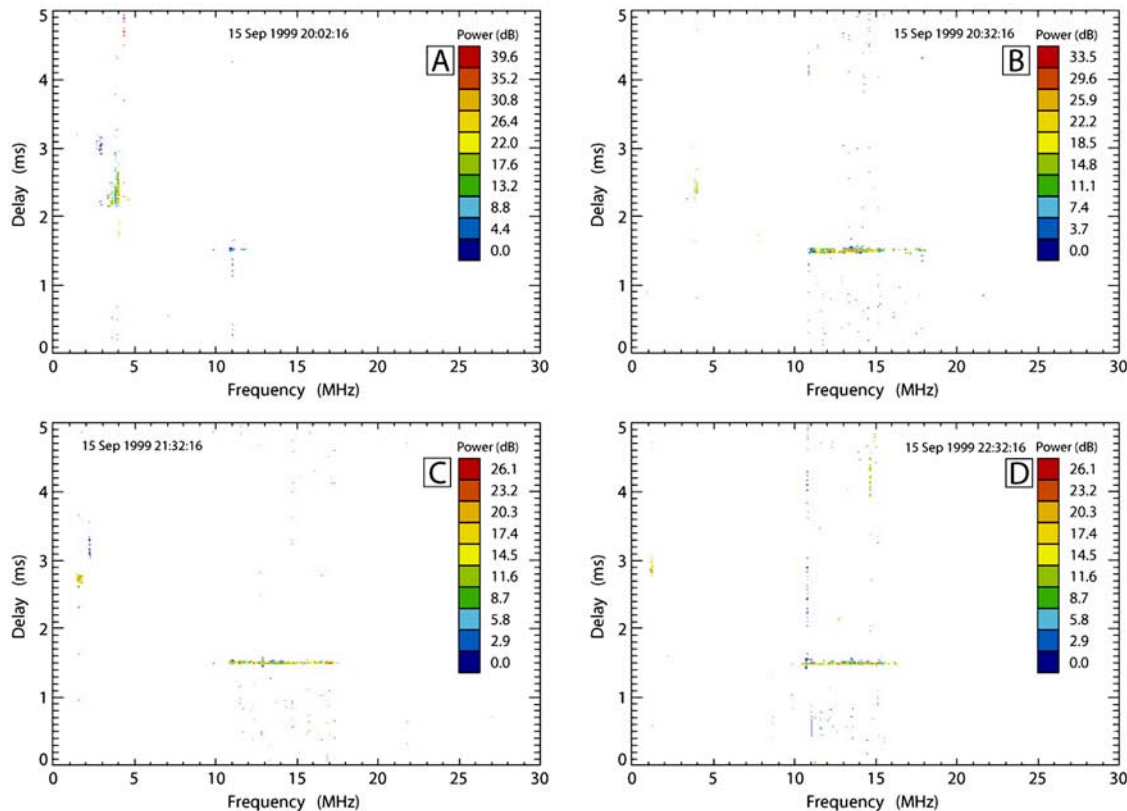


Figure 13. Selection of oblique ionograms from the Svalbard to Malvern path. (The x axis is frequency in MHz, and the y axis is virtual height in km.)

required.  $F_oE_s$  is already above the norm at 3 MHz at this stage.

[58] Figure 14b is 11 min after the SSC occurs the  $E_s$  layer is dramatically enhanced and almost completely blankets the  $F$  region. Here  $f_oE_s$  is 2.9 MHz with a  $F$  region window of only 0.5 MHz between 3 – 3.5 MHz. Figure 14c is the situation continues and more than 1 h later, in the 21:24UT ionogram, a similar situation exists with  $F_oE_s = 3.1$  MHz which is sufficient to completely blanket the  $F$  region. Interestingly in this case we do not see the large increases in virtual  $F$  layer heights as seen in the first case study.

[59] The virtual height of the  $F$  layer (>400 km, Figure 14) before and after the SSC, the low frequencies seen on the oblique high raypath (>2ms, Figure 13) and the  $28^\circ$  take off angle required; fits in well with the considered view that a 2F mode occurs normally instead of a 1F mode on this path. As the length of the path prohibits a 1E mode of propagation, a 2E mode with a take off angle of  $5^\circ$  dominates following the SSC.

[60] Figure 15 is a selection of ionograms from the Gakona Ionosonde which captured events around the SSC that occurred at 0753 UT. This ionosonde, located on the other side of the polar cap from the link transmitter is included to show the extent of the ionospheric disturbance following the SSC.

[61] Figure 15a is a fairly disturbed early morning ionogram where trace spread makes it difficult to extract any accurate parameters, however  $f_oF$  is approximately 3.2 MHz and  $f_oE_s$  is approximately 2.8 MHz. It is difficult to determine  $h'f$  from the ionogram. Figure 15b is 37 min after the SSC a dense sporadic  $E$  layer has formed which almost completely blankets the  $F$  region,  $f_oE_s$  has extended to 5.5 MHz. The second reflection from the  $E$  layer is visible at a height of 220 km and a small reflection is visible from the  $F$  layer at a height of 280 km. Figure 15c is the now fully blanketing  $E_s$  layer continues for at least another 2 h after SSC, albeit slightly patchy at the top end.

## 5. Conclusions

[62] Six different instruments have been utilized in these case studies to show the cause and effect of enhanced  $E_s$  layers immediately following an SSC. These studies demonstrate the profound effects these sporadic layers have on high-latitude HF circuits by dramatically extending the  $E$  layer maximum usable frequency (MUF) and/or “shielding” any  $F$  layer raypaths.

[63] Data from the ACE satellite is used to show the magnitude of changes that occur in the solar wind due to disturbances in the solar wind, such as when shock waves and dynamic pressure pulses move past the satellite on

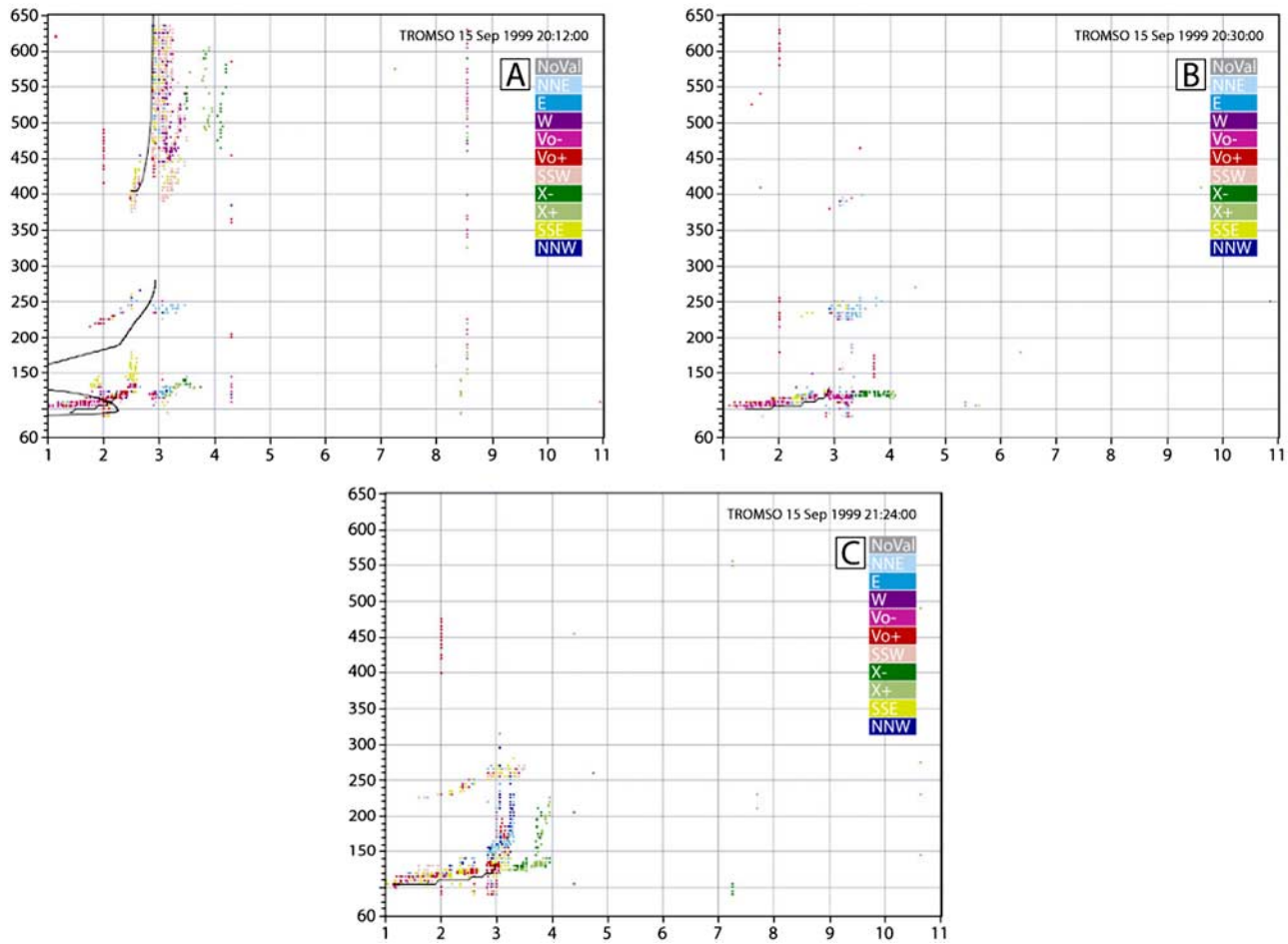


**Figure 14.** Selection of vertical ionograms from the Tromsø ionosonde. (The x axis is frequency in MHz, and the y axis is virtual height in km.)

their way to impinging on the Earth's magnetosphere. The step changes in total magnetic field strength, particle density and velocity as well as changes in direction of the  $B_z$  component are shown. The direction of  $B_z$  changes from south to north in the first case study but starts northward and becomes progressively more northward in the second case study. Changes in the ground-based geomagnetic field intensity due to an increase in magnetopause current, as a result of magnetospheric compression caused by solar wind disturbances, are seen in the magnetometer data.

[64] The observation of sudden changes in the solar wind which are the cause of SSC is well understood as is the prediction of the time delay between observation by the ACE satellite platform and the arrival of the disturbance at the Earth's surface. The SSC event is used as a proxy to herald the change between a "quiet" and a "disturbed" high-latitude ionosphere and the subsequent onset of an enhanced  $E$  layer. However, for the first time the linkage between SSC and the enhanced  $E$  layer ionisation is exposed in both case studies detailed in this paper.

[65] Ionosonde records show how the usefulness of the  $F$  layer is reduced as its electron density decreases and its virtual height increases following disturbances initiated by the SSC. The records further show the enhancement of the  $E_s$  layer for extended periods, in both cases for at least 2 h and in one case as long as 3 h. The enhancement is so great in some cases that the  $F$  layer is completely screened off from the ground. The Tromsø ionosonde, close to the center of the first case study link path demonstrates the change that occurs in the height of the  $F$  layer around the single reflecting control point. This knowledge allows a more realistic ray tracing geometry to be used when attempting to model and predict propagation during such disturbances.

[66] The ISR records reveal the sudden enhancement of electron density in the  $E$  region coincident with the SSC as well of the scale of the increase in electron density that can be expected. The affect of storms and substorms on the significant modulation of electron density at  $E_s$  altitudes is clearly demonstrated. The ISR records support the longevity of enhancement of the  $E_s$  layer electron density that is seen in the ionosonde and oblique sounder records.

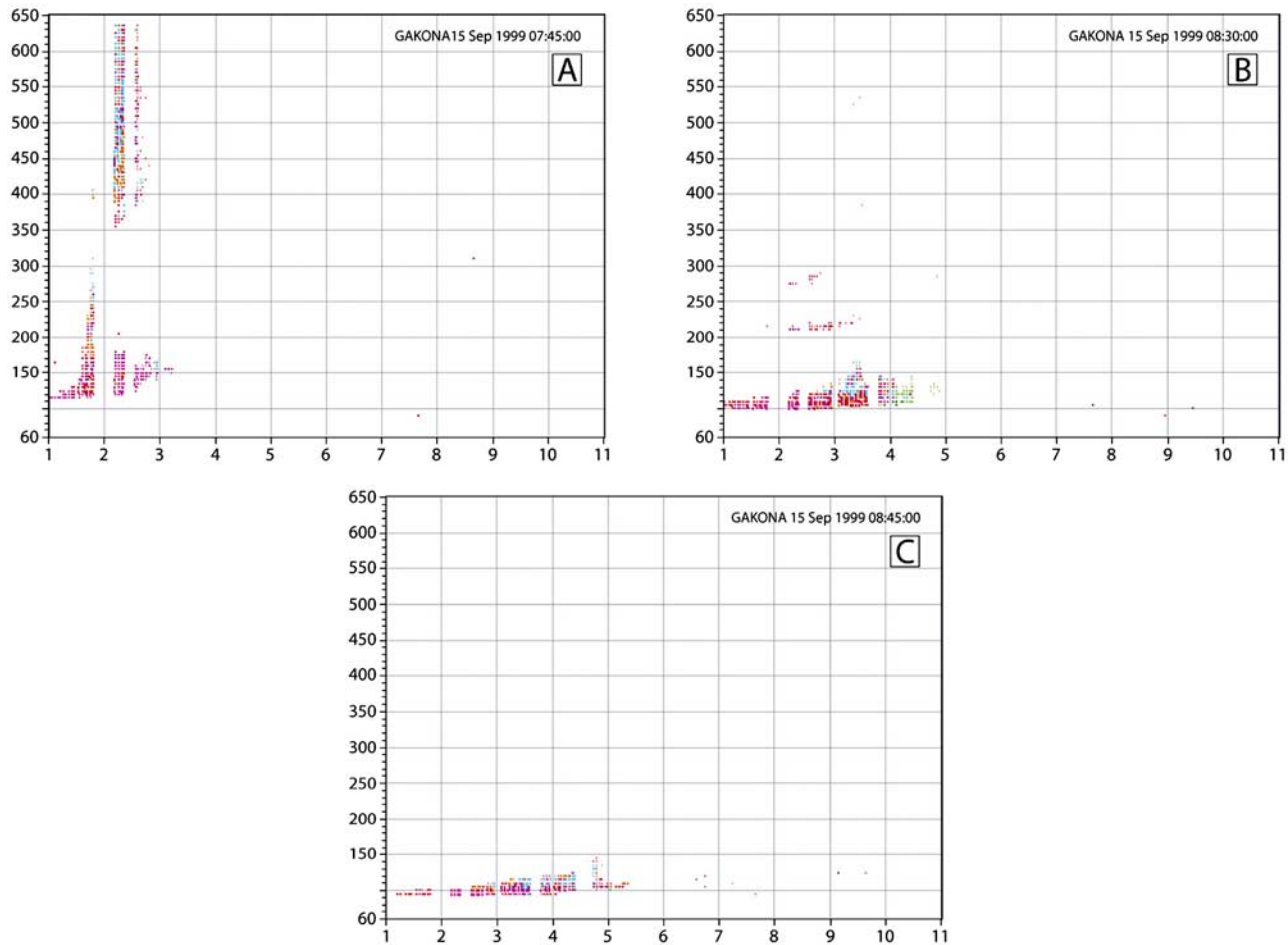


**Figure 15.** Selection of vertical ionograms from the Gakona ionosonde. (The x axis is frequency in MHz, and the y axis is virtual height in km.)

[67] The change in cosmic radio noise absorption as measured by a riometer reflects the effect of particle precipitation on the  $D$  layer and supports the interpretation of the ionosonde and oblique sounder data. There is good correlation of the affect of absorption, as expected, between the oblique sounder, the Tromso ionosonde and the riometer measuring the absorption.

[68] Key to both case studies are records from the oblique sounder which reveals the practical effects of an enhanced  $E_s$  layer. The majority of all HF communication links are planned assuming the use of the  $F_2$  layer as the refracting layer as well as assuming a fixed reflection height (normally 250 km). A HF system designed to reach a particular point or area such as point-to-point links and targeted broadcasting use complex antennas that concentrate the radiated power in both azimuth and elevation. These two assumptions are perfectly valid when dealing with a quiet ionosphere. However, the variations in the height of the  $F$  layer, the reduction of the height of the expected reflecting layer from 250 km to 100 km as well as the phenomena of the  $E_s$  layer screening the  $F$  layer, has severe implications. This can be seen when examining

Figures 9 and 10. Figure 10 shows the modified geometry for a number of different modes at three different fixed heights (300, 350, and 450 km). The change in reflection layer from the  $F$  to the  $E_s$  layer has the most drastic effect as the elevation angle changes from a maximum peak of  $22^\circ$  at  $h'F$  of 450 km to a low of  $3^\circ$  at  $h'E$  of 110 km. For many types of specialist antenna this change is greater than the available elevation beam width. The change in  $h'F$  from 250 to 450 km and the corresponding elevation angle modification from  $11^\circ$  to  $22^\circ$  has similar antenna issues.

[69] Following an SSC event or during magnetic storms, one rational approach toward using the ionosphere for HF communications in high-latitude regions is to rely solely on  $E$  layer modes and to provide higher power or increased antenna gain in bands appropriate for  $E_s$  layer propagation. Overcoming these problems may prove to be economically challenging for operators of fixed links and broadcasting services. However, with relevance to tactical links and safety of life transmissions, the oblique sounder reveals, counter intuitively perhaps, that instead of reducing the frequency of operation to reestablish disrupted links, it would be better to increase the frequency of

operation to fully utilize the enhanced  $E$  layer while overcoming some of the affects of absorption. In the first case study, before the SSC occurs the  $F$  layer can support reflections from 6 to 11 MHz over this link while the  $E_s$  layer is supporting reflections between 10 and 15 MHz after the SSC. Twenty min after the SSC there is sporadic reflections from the  $F$  layer but the  $E_s$  layer is now capable of supporting a number of paths using frequencies between 12 and 20 MHz. During this period of approximately 1 h any attempt to reestablish a link by reducing the operating frequency would be futile. The oblique ionogram shows no link paths are available on this circuit if the frequency is reduced. The only solution is to increase the operating frequency, by more than 5 MHz, in order to reestablish the link. The same principle is clearly shown in the second case study where the only manner in which a link can be established in the 2 h following the SSC event is for the operator to increase frequency by more than 7 MHz to be able to utilize the  $E_s$  layer for communications. As explained, in order to implement this mitigation technique, equipment at both ends of the link will need to be sufficiently frequency agile and have access to antenna with takeoff angles appropriate for  $E_s$  layer operation.

[70] Both case studies demonstrate: the effect of the ionospheric disturbance that is an enhanced  $E_s$  layer that dominates the mode of propagation, the durability of the enhanced  $E_s$  layer allowing the reestablishment of a reliable reflecting layer following the demise of the  $F$  layer and the viability of using the  $E_s$  layer in supporting HF communications at high latitudes. Following up on the last point, the extent of the enhanced  $E_s$  layer is evident in the second case study. A  $2E$  mode of propagation is relied on over the 3000 km path which requires two  $E_s$  layer reflections spaced 1500 km apart, this is confirmed by ISR data showing similar enhancements in different sectors.

[71] From an operational point of view a technique is needed to address the uncertainties generated by ionospheric disturbances on key ionospheric parameters and a number of authors have examined this problem [e.g., Tsagouri et al., 2005; I. Barnes et al., Real time ionospheric models for the Australian Defense Force, paper presented at Workshop on the Applications of Radio Science, La Trobe University, Beechworth, Victoria, Australia, 27–29 April, 2000; R. J. Norman et al., A HF ionospheric propagation model using analytic ray tracing, paper presented at Colloquium on HF Antennas and Propagation, Institution of Electrical Engineers, London, 14 November, 1995; R. Gardiner-Garden et al., Modeling uncertainty in a real-time model (nowcast) of the ionosphere, paper presented at 12th International Ionospheric Effects Symposium, Office of Naval Research, Air Force Office of Scientific Research, and International Union of Radio Science, Alexandria, Virginia, 13–15 May, 2008]. A number of authors have proposed the use of oblique and vertical sounding data to provide near real-time ionospheric maps and communication performance parameters [e.g., Zolesi et al., 2004; J. M. Goodman and J. W.

Ballard, Dynamic management of HF communication and broadcasting systems, paper presented at Colloquium on Frequency Selection and Management Techniques for HF Communications, Institution of Electrical Engineers, London, 1999]. Certainly while each of these approaches has different applications and merits, the authors have chosen another approach.

[72] The use of propagation prediction programs to establish, in advance, the choice of operating frequency is still the basis of many operations. For example HF broadcasting requires frequencies and schedules to be agreed months in advance of actual usage and military exercises at high latitudes are preceded by detailed advance planning and the distribution of set tables of frequencies well in advance. It appears that this methodology of advance planning is good enough for operational use and that the range of parameters produced by the propagation prediction programs is adequate for operational purposes, during quiet conditions. The problem to be overcome is to determine what propagation parameters need to be modified during disturbed conditions, that is, what consequential modifications need to be made to the communications system to ensure some form of continued operation during disturbed conditions.

[73] The authors' approach is that advocated by Lundborg et al. [1995], "It seems that priority should be given to the development of propagation prediction methods which predict the deviation from the median rather than the median." Following research into disturbances affecting the  $D$  region the median increase in absorption that needs to be taken into account following an SSC has now been empirically determined [Ritchie and Honary, 2009a]. An investigation into disturbances affecting the  $E$  region has led to the characterization of the change in the median value of the critical frequency of  $E_s$  and the occurrence of fully blanketing  $E_s$  follow an SSC [Ritchie and Honary, 2009b]. This paper details the deviation of  $f_oE_s$  (from its quiet ionosphere value) for the 4 h immediately following the SSC and establishes a threshold of deviation that predicts the onset of fully blanketing  $E_s$ . The strength of this approach is that system operators can adjust for the deviation of critical frequencies from the quiet ionosphere predictive norm following SSC and the onset of storms, without the need for a supporting network of vertical and/or oblique sounders.

[74] **Acknowledgments.** This research is supported by the first author's employer, the Commission for Communications Regulation (ComReg), Dublin, Ireland. The authors thank the Radio and Science Plasma Physics Group at the University of Leicester for the use of the oblique sounder data and the SAMNET team for the magnetometer data. The Sub-Auroral Magnetometer Network data (SAMNET) is operated by the Department of Communications Systems at Lancaster University (UK) and is funded by the Science and Technology Facilities Council (STFC). The authors acknowledge Qinetiq

for the use of the Tromso Ionosonde data, the U.S. Airforce Laboratory for the use of the Gakona Ionosonde data, the Lowell DIDBase project for access to the ionosonde database [Reinisch et al., 2004], and Mary McCready (SRI) and Andrew Kavanagh (University of Lancaster) for assistance in preparing print quality graphics. The authors also acknowledge the Sondrestrom Research Facility in Greenland for data from the IS radar at the facility and EISCAT for data from the Svalbard IS Radar. The Sondrestrom Radar measurements and analysis are supported under cooperative agreement ATM-0334122 between the U.S. National Science Foundation and SRI International. EISCAT is an international association supported by the research councils of Finland (SA), France (CNRS), the Federal Republic of Germany (MPG), Japan (NIPR), Norway (NFR), Sweden (VR), and the United Kingdom (STFC).

## References

- Araki, T. (1977), Global structure of geomagnetic sudden commencements, *Planet. Space Sci.*, 25, 373–384, doi:10.1016/0032-0633(77)90053-8.
- Baron, M. J. (1974), Electron densities within aurora and other auroral E region characteristics, *Radio Sci.*, 9(2), 341–348, doi:10.1029/RS009i002p00341.
- Bates, H. F., and R. D. Hunsucker (1974), Quiet and disturbed electron density profiles in the auroral zone ionosphere, *Radio Sci.*, 9(4), 455–467, doi:10.1029/RS009i004p00455.
- Blagoveshchensky, D. V., V. M. Vystavnoi, and M. A. Sergeeva (2005), HF radio propagation through the auroral oval during substorms, *J. Atmos. Sol. Terr. Phys.*, 67, 1618–1625, doi:10.1016/j.jastp.2005.08.022.
- Blagoveshchensky, D. V., A. S. Kalishin, and M. A. Sergeeva (2008), Space weather effects on radio propagation: Study of the CEDAR, GEM and ISTP storm events, *Ann. Geophys.*, 26, 1479–1490.
- Bröms, M., and B. Lundborg (1994), Results from Swedish oblique soundings campaigns, *Ann. Geophys.*, XXXVII(2), 145–152.
- Browne, S., J. K. Hargreaves, and B. Honary (1995), An imaging riometer for ionospheric studies, *Electron. Commun. Eng. J.*, 7, 209–217.
- Buonsanto, M. J. (1999), Ionospheric storms—A review, *Space Sci. Rev.*, 88, 563–601, doi:10.1023/A:1005107532631.
- Burlaga, L. F., and K. W. Ogilvie (1969), Causes of sudden commencements and sudden impulses, *J. Geophys. Res.*, 74, 2815–2825.
- Davies, K. (1965), *Ionospheric Radio Propagation*, *Natl. Bur. Stand. Monogr. Ser.*, vol. 80, chapter 4, pp. 165–192, Dover, New York.
- Davies, K. (1991), *Ionospheric Radio*, *Inst. Electr. Eng. Electromagn. Wave Ser.*, vol. 31, Peter Peregrinus, London.
- Fairfield, D. H. (1971), Average and unusual locations of the Earth's magnetopause and bow shock, *J. Geophys. Res.*, 76, 6700–6719, doi:10.1029/JA076i028p06700.
- Ferraro, V. C. A., W. C. Parkinson, and H. W. Unthank (1951), Sudden commencement and sudden impulses in geomagnetism: Their hourly frequency at Cheltenham (MD.), Tucson, San Juan, Honolulu, Huancayo and Watheroo, *J. Geophys. Res.*, 56, 177–195, doi:10.1029/JZ056i002p00177.
- Goodman, J. M. (1991), *H. F. Communications: Science and Technology*, Nostrand Reinhold, New York.
- Goodman, J. M., and J. W. Ballard (2004), An examination of elevated frequency propagation over a transpolar path, *Radio Sci.*, 39, RS1529, doi:10.1029/2002RS002850.
- Goodman, J. M., J. W. Ballard, and E. Sharp (1997), A long term investigation of the HF communication channel over middle- and high-latitude paths, *Radio Sci.*, 32(4), 1705–1715, doi:10.1029/97RS01194.
- Hargreaves, J. K. (1969), Auroral absorption of HF radio waves in the ionosphere: A review of results from the first decade of riometry, *Proc. IEEE*, 57, 1348–1373, doi:10.1109/PROC.1969.7275.
- Hunsucker, R. D. (1999), Final report on PENEX data analysis project for the Naval Postgraduate School, report, Nav. Postgrad. Sch., Monterey, Calif.
- Hunsucker, R. D., and H. F. Bates (1969), Surevy of polar and auroral region effects on HF propagation, *Radio Sci.*, 4(4), 347–365, doi:10.1029/RS004i004p00347.
- Hunsucker, R. D., and J. K. Hargreaves (2003), *The High Latitude Ionosphere and Its Effects on Radio Propagation*, Cambridge Univ. Press, Cambridge, U. K.
- International Service of Geomagnetic Indices (2008), Service International des Indices Geomagnetiques, <http://isgi.cetp.ipl.fr/lesdonne.htm>, Paris.
- Ivanov, V. A., V. I. Kurkin, V. E. Nosov, V. P. Uryadov, and V. U. Shumaev (2003), Chirp ionosonde and its application in the ionospheric research, *Radiophys. Quantum Electron.*, 46(11), 821–851, doi:10.1023/B:RAQE.0000028576.51983.9c..
- Jull, G. W. (1964), HF propagation in the arctic, in *Arctic Communications*, edited by B. Landmark, chapter 15, pp. 157–176, Pergamon, New York.
- Kaufmann, R. L., and A. Konradi (1969), Explorer 12 magnetopause observations: large-scale nonuniform motion, *J. Geophys. Res.*, 74, 3609–3627, doi:10.1029/JA074i014p03609.
- Lane, G. (2001), *Signal-to-Noise Predictions Using VOACAP, Including VOAREA—A Users Guide*, Rockwell Collins, Cedar Rapids, Iowa.
- Leid, F. (1967), *High Frequency Radio Communications With Emphasis on Polar Problems*, *Advis. Group Aerosp. Res. Dev. Monogr. Ser.*, vol. 104, Technivision, Maidenhead, U. K.
- Little, C. G., and H. Leinbach (1959), The riometer—A device for the continuous measurements of ionospheric absorption, *Proc. Inst. Radio Eng.*, 37, 315–320.
- Lundborg, B., M. Bröms, and H. Derblom (1995), Oblique sounding of an auroral ionospheric HF channel, *J. Atmos. Terr. Phys.*, 57(1), 51–63, doi:10.1016/0021-9169(93)E0020-A.
- McNamara, L. F. (1991), *The Ionosphere: Communications, Surveillance and Direction Finding*, Krieger, Malabar, Fla.
- NOAA (1999a), Space weather highlights for 26 July–01 Aug 1999, Rep. SWO PRF 1248, Washington, D. C.
- NOAA (1999b), Space weather highlights for 13–19 September 1999, Rep. SWO PRF 1255, Washington, D. C.
- Owren, L., J. Ortner, K. Folkestad, and R. Hunsucker (1963), Arctic propagation studies at ionospheric modes of propagation, *Final Rep. AF 19(604)–5574*, Geophys. Inst. of the Univ. of Alaska, Fairbanks, Alaska.
- Piggott, W. R., and R. Rawer (1972), URSI handbook of ionogram interpretation and reduction, *Rep. UAG-23*, NOAA, Boulder, Colo.
- Ranta, A., and H. Ranta (1990), Storm sudden commencements observed in ionospheric absorption, *Planet. Space Sci.*, 38(3), 365–372, doi:10.1016/0032-0633(90)90102-V.
- Rastogi, R. G., B. M. Pathan, D. R. K. Rao, T. S. Sastry, and J. H. Sastri (2001), On latitudinal profile of storm sudden commencement in H, Y and Z at Indian Geomagnetic Observatory chain, *Earth Planets Space*, 53, 121–127.
- Rees, M. H. (1963), Auroral ionisation and excitation by incident energetic electrons, *Planet. Space Sci.*, 11, 1209–1218, doi:10.1016/0032-0633(63)90252-6.
- Reinisch, B. W. (1996), Modern ionosondes, in *Modern Ionospheric Science*, edited by H. Kohl, R. Rüster, and K. Schlegel, pp. 440–458, Eur. Geosci. Union, Strasbourg, France.
- Reinisch, B. W., I. A. Galkin, G. Khmyrov, A. Kozlov, and D. F. Kitrosser (2004), Automated collection and dissemination of ionospheric data from the Digisonde network, *Adv. Radio Sci.*, 2, 241–247.
- Ritchie, S. E., and F. Honary (2009a), Observed characteristics of sudden commencement absorption, *J. Atmos. Sol. Terr. Phys.*, 71(5), 609–617, doi:10.1016/j.jastp.2008.11.011.
- Ritchie, S. E., and F. Honary (2009b), Observations on the variability and screening effect of sporadic E, *J. Atmos. Sol. Terr. Phys.*, doi:10.1016/j.jastp.2009.05.008, in press.

- Russell, C. T., M. Ginskey, and S. M. Petrinec (1994), Sudden impulses at low-latitude stations: Steady state response for northward interplanetary magnetic field, *J. Geophys. Res.*, *99*(A1), 253–262, doi:10.1029/93JA02288.
- Stone, E. C., A. M. Frandsen, R. A. Mewaldt, E. R. Christian, D. Margolies, J. F. Ormes, and F. Snow (1998), The Advanced Composition Explorer, *Space Sci. Rev.*, *86*(1/4), 1–22, doi:10.1023/A:1005082526237.
- Takeuchi, T., C. T. Russell, and T. Araki (2002), Effect of the orientation on interplanetary shock on the geomagnetic sudden commencement, *J. Geophys. Res.*, *107*(A12), 1423, doi:10.1029/2002JA009597.
- Tamao, T. (1975), Unsteady interactions of solar wind disturbances with the magnetosphere, *J. Geophys. Res.*, *80*(31), 4230–4236, doi:10.1029/JA080i031p04230.
- Tsagouri, I., B. Zolesi, A. Belehaki, and L. R. Cander (2005), Evaluation of the performance of the real-time updated simplified ionospheric regional model for the European area, *J. Atmos. Sol. Terr. Phys.*, *67*(12), 1137–1146, doi:10.1016/j.jastp.2005.01.012.
- Tsurutani, B. T., W. D. Gonzalez, A. L. C. Gonzalez, F. Tang, and J. K. Okada (1995), Interplanetary origin of geomagnetic activity in the declining phase of the solar cycle, *J. Geophys. Res.*, *100*(A11), 21,717–21,734, doi:10.1029/95JA01476.
- University of Leicester (2007), Svalbard Oblique Sounder Page, <http://www.ion.le.ac.uk/iris/index.html>, Leicester, U. K.
- Walker, J. K. (1972), Auroral ionosphere models, *J. Atmos. Sol. Terr. Phys.*, *34*, 1681–1689, doi:10.1016/0021-9169(72)90028-1.
- Wilken, B., C. K. Goertz, D. N. Baker, P. R. Higbie, and T. A. Fritz (1982), The SSC on July 29, 1977 and its propagation within the magnetosphere, *J. Geophys. Res.*, *87*(A8), 5901–5910, doi:10.1029/JA087iA08p05901.
- Wilken, B., D. N. Baker, P. R. Higbie, T. A. Fritz, W. P. Olsen, and K. A. Pfitzer (1986), Magnetospheric configuration and energetic particle effects associated with SSC: A case study of the CDAW 6 event on March 22, 1979, *J. Geophys. Res.*, *91*(A2), 1459–1473, doi:10.1029/JA091iA02p01459.
- Wright, J. W., R. W. Knecht, and K. Davies (1957), *Annals of the IGY, Vol. III, Part 1*, Pergamon, Oxford, U. K.
- Zesta, E., H. J. Singer, D. Lummerzheim, C. T. Russell, L. R. Lyons, and M. J. Brittner (2000), The effect of the January 10, 1997, pressure pulse on the magnetosphere-ionosphere current system, in *Magnetospheric Current Systems, Geophys. Monogr. Ser.*, vol. 118, edited by S. Ohtani et al., pp. 217–226, AGU, Washington, D. C.
- Zolesi, B., A. Belehaki, I. Tsagouri, and L. R. Cander (2004), Real-time updating of the Simplified Ionospheric Regional Model for operational applications, *Radio Sci.*, *39*, RS2011, doi:10.1029/2003RS002936.

---

F. Honary and S. E. Ritchie, Department of Communication Systems, University of Lancaster, Lancaster LA1 4W4, UK. (f.honary@lancaster.ac.uk; s.ritchie@lancaster.ac.uk)